Interference, dephasing, and vibrational coupling effects between coherence pathways in doubly vibrationally enhanced nonlinear spectroscopies

6 AUTHORS, INCLUDING:

Keith Murdoch
Coherent Inc.

38 PUBLICATIONS   **454** CITATIONS

Wei Zhao
University of Arkansas at Little Rock

76 PUBLICATIONS   **1,824** CITATIONS

Kent A Meyer
Oak Ridge National Laboratory

28 PUBLICATIONS   **270** CITATIONS

Interference, dephasing, and vibrational coupling effects between coherence pathways in doubly vibrationally enhanced nonlinear spectroscopies

Daniel M. Besemann, Nicholas J. Condon, Keith M. Murdoch, Wei Zhao,
Kent A. Meyer, John C. Wright *

Department of Chemistry, University of Wisconsin – Madison, 1101 University Avenue, Madison, WI 53706, USA

Abstract

Doubly vibrationally enhanced (DOVE) four-wave mixing is capable of producing coherent two-dimensional (2D) vibrational spectra with cross-peaks that reflect intramolecular and intermolecular mode coupling. These methods are based on double vibrational coherences that are analogous to the double spin coherences in 2D nuclear magnetic resonance methods. In particular, there are two pathways for DOVE infrared spectroscopy that interfere to change the line shapes of doubly resonant cross-peaks. The interference depends on the relative dephasing rates of the coherences involved in the different pathways. We derive relationships between the dephasing rates of the different coherences in DOVE pathways and show how these relationships affect the line shapes of DOVE resonances. Comparisons are made with experimental 2D DOVE spectra. © 2001 Elsevier Science B.V. All rights reserved.

Keywords: Two-dimensional nonlinear spectroscopy; Four-wave mixing; Multiresonant; Lineshapes; DOVE; Combination bands; Vibrational coupling

1. Introduction

Two-dimensional (2D) spectroscopic techniques play an important role in chemical measurements because they often provide the resolution and selectivity required for understanding complex samples. 2D laser spectroscopy can potentially provide

high selectivity – in the frequency domain through narrow spectral line widths of lasers and in the time domain through Fourier analysis of impulsively excited optical responses. In particular, 2D laser spectroscopy exhibits cross-peaks that identify transitions which are correlated, either because they are coupled by intramolecular or intermolecular interactions or because they have common origins on a specific component, conformer, isotopomer, or molecular environment of a sample. The first 2D laser methods were the Doppler free and Lamb dip spectroscopies that narrowed inhomogeneously broadened atomic transitions [1–3]. One laser frequency bleached a portion of

---
* Corresponding author. Tel.: +1-608-262-0351; fax: +1-608-262-0453.

E-mail address: wright@chem.wisc.edu (J.C. Wright).

the inhomogeneous Doppler broadened profile while a second laser frequency probed the bleached population. Selectivity was extended to solid materials and organic glasses using fluorescence line narrowing, hole burning, and site selective spectroscopy [4].

The traditional pump–probe methods are based on selectively perturbing populations and looking for differences in absorption transitions [5]. Since one frequency affects the optical properties sensed at a different frequency, the absorption differences in pump–probe methods are a form of 2D spectroscopy [6,7]. Another approach is based on using the multiple resonances of coherent nonlinear spectroscopy to drive doubly excited coherences [8–11]. A coherence is a time dependent state that is a linear combination of two states so a coherence involving states b and a is proportional to the off-diagonal density matrix element, ρ_{ba}. Rather than sensing differences in absorption transitions, the doubly excited coherences can be detected directly by the light they emit. Early work used traditional coherent anti-stokes Raman scattering (CARS) methods to simultaneously excite doubly excited coherences that involved both a ground state vibrational level and an excited electronic state's vibronic level [12]. Subsequent work used fully resonant four-wave mixing (FWM) to achieve component selectivity [13,14], inhomogeneous line narrowing [15–18], and selectivity to mode coupling [19–22].

Nonlinear methods were usually limited to electronic transitions because the nonlinear electronic polarizability is much larger than the nuclear polarizability and the vibrational contributions are negligible [23]. However, if one is resonant with vibrational transitions, the nuclear polarizability is enhanced so it can dominate. This enhancement was used by Fayer and coworkers for observing vibrational echoes [24,25], by Hochstrasser and coworkers for observing pump–probe coherences [6,7,26], and by our group for observing nondegenerate vibrational FWM [10,11,27].

The coherent methods have a direct relationship to 2D nuclear magnetic resonance (NMR) methods such as COSY and NOESY that have a very high selectivity [28,29]. Many of the NMR methods are based on exciting double spin coherences

in systems where the spins are coupled by intramolecular or intermolecular interactions. Similarly, the vibrational analogue requires exciting double vibrational coherences where the vibrational modes are coupled by intramolecular or intermolecular interactions. Photon echo and optical nutation were the first optical analogues of NMR [30] but they were not commonly used because optical processes have picosecond coherent dephasing times for typical systems, much shorter than the millisecond dephasing times of spin coherences. Observation of these optical coherent signals required cryogenic temperatures or very low gas pressures to lengthen the dephasing times enough to create a series of $\pi/2$ and/or π pulses. Practical coherent methods become possible because the phase matching condition and time ordering of pulses in nonlinear spectroscopy act to select the particular process that has the proper series of interactions required for the coherent process. For example, although there are a plethora of nonlinear processes that can occur when several lasers are focused into a sample, it is well known that selection of the time ordering and the phase matching condition $\bar{k}_4 = -\bar{k}_1 + \bar{k}_2 + \bar{k}_3$ can select the stimulated photon echo process where $-\bar{k}_1$ creates a coherence, ρ_{ga} from a ground state population, ρ_{gg}, $\bar{k}_2$ returns the coherence to a ground or excited state population, ρ_{gg} or ρ_{aa}, and $\bar{k}_3$ creates the conjugate coherence, ρ_{ag}. One then observes a photon echo even though one has not been careful to design coherent $\pi/2$ pulses [31]. In the same way, one can extend the stimulated photon echo process by creating doubly excited coherences like ρ_{cb} that are required for 2D spectroscopy. One does this by using a second pulse to excite state "g" in a ρ_{gb} or ρ_{cg} coherence to a ρ_{cb} coherence.

Our first attempt to observe a nonlinear spectroscopy with doubly excited vibrational coherences was based on frequency domain six wave mixing with two Raman excitations. This attempt (labeled CHORES for coherent higher order Raman excitation spectroscopy) failed because the six-wave mixing signal was obscured by cascaded FWM processes (labeled SCARS for sequential CARS) [32]. At the same time that this work was published, Tanimura and Mukamel proposed a

similar time domain six wave mixing 2D Raman process that also involved the doubly excited vibrational coherence [33]. Although initial experimental work reported observation of this process [34–36], later work showed that it experiences the same problems with cascaded FWM [37]. The most recent work suggests the cascaded FWM can be overcome with appropriate phase matching, heterodyne detection, and short sample pathlengths [38].

Since higher order processes are plagued by the cascaded processes, we turned to the lower order nonlinear spectroscopies that could still achieve a doubly excited coherence in analogy to the similar methods developed for multiresonant electronic FWM [39,40]. Collectively, they have been labeled doubly vibrationally enhanced (DOVE) spectroscopies [9]. There are many ways to create DOVE processes. The lowest order DOVE processes could appear in three wave mixing spectroscopies based on $\chi^{(2)}$ such as sum and difference frequency generation. The $\chi^{(2)}$ processes have two resonances that are excited by tuning to absorption transitions between vibrational states. These processes and all other odd wave mixing processes would be surface

selective since they vanish for systems with inversion symmetry.

Fig. 1 shows representative time orderings of the DOVE processes that are possible for FWM spectroscopies based on $\chi^{(3)}$ [9]. All the states in the figure are represented with solid lines to indicate possible resonances (they could also represent virtual levels). The top row of processes is experimentally convenient because the output signals have higher frequencies than those from the bottom row, which would generally be in the infrared (IR) and would be harder to detect efficiently. The characteristics of these different processes are described elsewhere [9]. We concentrate on the first process in Fig. 1a (called DOVE-IR) which involves two IR absorptions and a Raman process, and the process shown in Fig. 1c (called DOVE-Raman) which involves a vibrationally enhanced Raman process followed by a second Raman process. In addition to FWM, there are analogous DOVE processes that can occur in higher and lower orders. Higher order processes may play an important role in future developments of multidimensional spectroscopies because they will provide capabilities analogous to
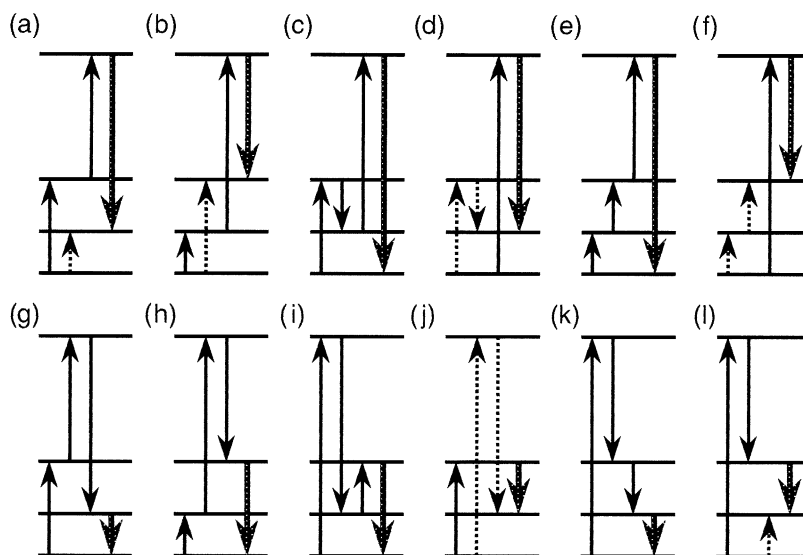

Fig. 1. Summary of the WMEL diagrams for the different FWM DOVE processes that are possible. The numbers label the excitation frequencies. The solid arrows indicate ket-side transitions, the dotted arrows indicate bra-side transitions, and the larger arrows indicate the output transition.

multipulse NMR methods. The SWM Raman experiment is an example of a higher order process [32].

The DOVE-IR and DOVE-Raman experiments are performed by focusing two tunable IR and one visible or UV beam into a sample [41]. The angles between the beams are adjusted for optimum phase matching. Nonlinear FWM creates new beams at all the possible combinations of three frequencies. The directions of the output beams are dictated by the phase matching conditions. Using the conventions shown in Fig. 2, the intensity of the beam that is created at $\vec{k}_4 = \vec{k}_1 - \vec{k}_2 + \vec{k}_3$ is isolated and measured.
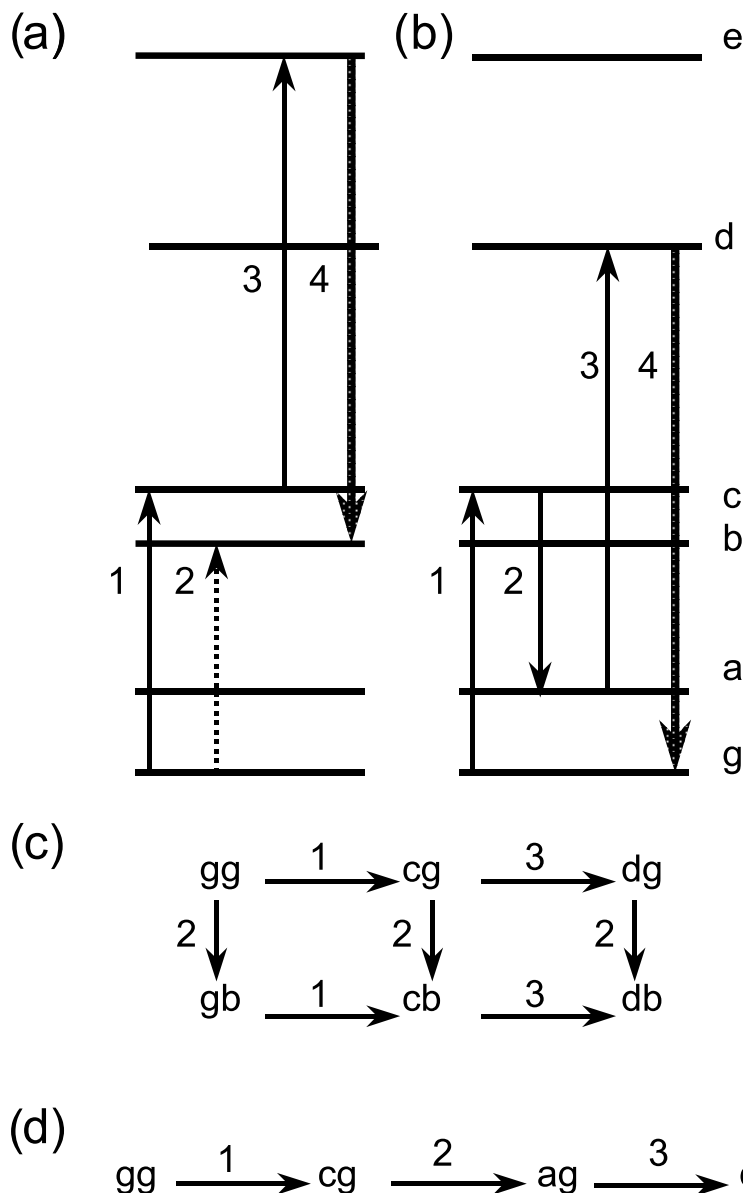

Fig. 2. (a) WMEL diagram for a DOVE-IR process. (b) WMEL diagram for a DOVE-Raman process. (c) The three coherent pathways for a DOVE-IR process. (d) The coherent pathway for a DOVE-Raman process.

Experimentally, singly vibrationally enhanced (SIVE) FWM was observed in 1997 [42] and DOVE FWM was observed in 1999 [10,27]. The capabilities for coherent 2D DOVE methods to both selectively probe specific components and coupled vibrational modes and to eliminate spectral congestion have been demonstrated in the 2D DOVE spectra [11,27,43,44]. In addition, the line shapes in the 2D spectra carry information about interferences between the different nonlinear polarizations that are created in the experiment [45]. In this paper, we explore the role of different coherent pathways in DOVE methods in determining the line shapes that are observed in 2D spectra.

2. Background and theory

2.1. Introduction

Density matrix theory is a convenient description of the dynamic processes in coherent 2D vibrational spectroscopies [31]. A coherence is a time dependent superposition of two states, α and β, defined by

$$\Psi_{\alpha,\beta}(\bar{x},t) = c_\alpha(t)|\psi_\alpha(\bar{x})\rangle + c_\beta(t)|\psi_\beta(\bar{x})\rangle, \qquad (1)$$

where the coefficients of the wave functions carry all the temporal information. Off-diagonal density matrix elements defined by

$$\rho_{\alpha\beta} \equiv c_\alpha c_\beta^*, \qquad (2)$$

provide a measure of the coherence, while the diagonal $\rho_{\alpha\alpha}$ provide a measure of the α state population. If a field is turned on and it induces a transition between states α and γ, the $\rho_{\alpha\beta}$ coherence changes into a coherence $\rho_{\gamma\beta}$. If one starts at $t = 0$ with a steady state coherence that is driven by a series of laser fields,

$$\rho_{\alpha\beta} = \rho_{\alpha\beta}^0 \exp[i(k_{\text{lasers}}z - \omega_{\text{lasers}}t)], \qquad (3)$$

one can show in the weak field limit that the relationship between the initial and final coherences is

$$\rho_{\gamma\beta} = \frac{\Omega_{\alpha\gamma}\rho_{\alpha\beta}^0}{2} \left\{ \frac{\exp\{i[(k_{\text{lasers}} + k)z - (\omega_{\text{lasers}} + \omega)t]\}}{\omega_{\gamma\beta} - (\omega_{\text{lasers}} + \omega) - i\Gamma_{\gamma\beta}} \right.$$
$$+ \frac{\exp\{i[(k_{\text{lasers}} - k)z - (\omega_{\text{lasers}} - \omega)t]\}}{\omega_{\gamma\beta} - (\omega_{\text{lasers}} - \omega) - i\Gamma_{\gamma\beta}}$$
$$+ \exp(-\Gamma_{\gamma\beta}t)\exp(-i\omega_{\gamma\beta}t)$$
$$\times \left(-\frac{\exp(i(k_{\text{lasers}} + k)z)}{\omega_{\gamma\beta} - (\omega_{\text{lasers}} + \omega) - i\Gamma_{\gamma\beta}} \right.$$
$$\left. \left. -\frac{\exp(i(k_{\text{lasers}} - k)z)}{\omega_{\gamma\beta} - (\omega_{\text{lasers}} - \omega) - i\Gamma_{\gamma\beta}} \right) \right\}$$
$$+ \rho_{\gamma\beta}(t = 0)\exp(-\Gamma_{\gamma\beta}t)\exp(-i\omega_{\gamma\beta}t), \qquad (4)$$

where $E = E^0/2(\exp[i(kz - \omega t)] + \exp[-i(kz - \omega t)])$ is the field inducing the transition, $\Omega_{\alpha\gamma}$ is the Rabi frequency ($\Omega_{\alpha\gamma} = \mu_{\alpha\gamma}E^0/\hbar$), $\mu_{\alpha\gamma}$ is the electric dipole moment of the $\alpha \to \gamma$ transition, k_{lasers} and ω_{lasers} are the combinations of excitation wave vectors and frequencies that created the $\rho_{\alpha\beta}$ coherence, and $\omega_{\gamma\beta}$ and $\Gamma_{\gamma\beta}$ are the frequency and dephasing rate of the $\rho_{\gamma\beta}$ coherence. These expressions are valid as long as $\Omega_{\alpha\gamma} \ll \Gamma_{\gamma\beta}$. The first two terms are the steady state values of the $\rho_{\gamma\beta}$ coherence and the last three terms are the transients. In the rotating wave approximation, two of the first four terms can be neglected depending upon whether the denominator $\omega_{\gamma\beta} - (\omega_{\text{lasers}} + \omega)$ or $\omega_{\gamma\beta} - (\omega_{\text{lasers}} - \omega)$ is closer to resonance.

The previous example involved a ket-side transition. Similarly, for a bra-side transition where state β undergoes a transition to state γ, the relationship between the initial $\rho_{\alpha\beta}$ coherence and the final $\rho_{\alpha\gamma}$ coherence is

$$\rho_{\alpha\gamma} = \frac{\Omega_{\beta\gamma}\rho_{\alpha\beta}^0}{2} \left\{ \frac{\exp\{i[(k_{\text{lasers}} + k)z - (\omega_{\text{lasers}} + \omega)t]\}}{\omega_{\gamma\alpha} + (\omega_{\text{lasers}} + \omega) + i\Gamma_{\gamma\beta}} \right.$$
$$+ \frac{\exp\{i[(k_{\text{lasers}} - k)z - (\omega_{\text{lasers}} - \omega)t]\}}{\omega_{\gamma\alpha} + (\omega_{\text{lasers}} - \omega) + i\Gamma_{\gamma\beta}}$$
$$+ \exp(-\Gamma_{\gamma\alpha}t)\exp(i\omega_{\gamma\alpha}t)$$
$$\times \left(-\frac{\exp(i(k_{\text{lasers}} + k)z)}{\omega_{\gamma\alpha} + (\omega_{\text{lasers}} + \omega) + i\Gamma_{\gamma\alpha}} \right.$$
$$\left. \left. -\frac{\exp(i(k_{\text{lasers}} - k)z)}{\omega_{\gamma\alpha} + (\omega_{\text{lasers}} - \omega) + i\Gamma_{\gamma\beta}} \right) \right\}$$
$$+ \rho_{\alpha\gamma}(t = 0)\exp(-\Gamma_{\gamma\alpha}t)\exp(i\omega_{\gamma\alpha}t). \qquad (5)$$

Note the difference in sign on the imaginary part of the denominators between Eqs. (4) and (5). This

difference leads to a π phase shift between the two coherences that is responsible for the refocusing in echo experiments. If states α and β are the same, the two coherences are conjugates.

Eqs. (4) and (5) hold in the limit of weak fields. In strong fields where the Rabi frequencies are much larger than the dephasing rates ($\Omega_{\alpha\gamma} \gg \Gamma_{\gamma\beta}$), coherences can evolve more fully. On resonance, one can write

$$c_\alpha = \cos(\Omega t/2)\exp(i\omega_\alpha t) \quad \text{and}$$
$$c_\beta = -i\sin(\Omega t/2)\exp(i\omega_\beta t). \tag{6}$$

These expressions describe optical nutation. Absorption occurs as the coherence evolves from the α state population towards an excited state population in state β, during times when $0 < \Omega t < \pi$. Emission occurs as the coherence evolves from the β state population towards the ground state population in state α, during times when $\pi < \Omega t < 2\pi$. If the excitation period is such that $\Omega t = \pi/2$, the largest coherence is produced where $|c_\alpha| = |c_\beta|$. For $\Omega t = \pi$, an initial α state population is converted to a β state population.

The different coherence pathways for DOVE-IR and DOVE-Raman are shown in Fig. 2. There are three time orderings for DOVE-IR and only one for DOVE-Raman. The $gg \rightarrow cg \rightarrow cb \rightarrow eb$ and $gg \rightarrow gb \rightarrow cb \rightarrow eb$ DOVE-IR pathways both involve two vibrational resonances and make the largest contributions if there are no resonances with the electronic (labeled e) state. The DOVE-Raman process has two vibrational resonances and a single $gg \rightarrow cg \rightarrow ag \rightarrow dg$ coherence pathway. These three pathways play the dominant role in our discussion of the DOVE experiments.

Successive use of Eqs. (4) and (5) can relate the final DOVE-IR coherence to the original population, ρ_{gg} [9]. In the rotating wave approximation, the steady state expression for the pathway $gg \rightarrow cg \rightarrow cb \rightarrow eb$ is

$$\rho_{eb}^\alpha = -\frac{\Omega_{gc}\Omega_{ce}\Omega_{gb}}{8\Delta_{cg}\Delta_{cb}\Delta_{eb}}\rho_{gg}\exp(i[[(k_1 - k_2 + k_3)z$$
$$- (\omega_1 - \omega_2 + \omega_3)t]), \tag{7}$$

where $\Delta_{cg} = \omega_{cg} - \omega_1 - i\Gamma_{cg}$, $\Delta_{cb} = \omega_{cb} - \omega_1 + \omega_2 - i\Gamma_{cb}$, and $\Delta_{eb} = \omega_{eb} - \omega_4 - i\Gamma_{eb}$. The expression for the pathway $gg \rightarrow gb \rightarrow cb \rightarrow eb$ is

$$\rho_{eb}^\beta = \frac{\Omega_{gc}\Omega_{ce}\Omega_{gb}}{8\Delta_{bg}^*\Delta_{cb}\Delta_{eb}}\rho_{gg}\exp(i[[(k_1 - k_2 + k_3)z$$
$$- (\omega_1 - \omega_2 + \omega_3)t]), \tag{8}$$

where $\Delta_{bg}^* = \omega_{bg} - \omega_2 + i\Gamma_{bg}$. Finally, the expression for DOVE-Raman is

$$\rho_{dg} = \frac{\Omega_{gc}\Omega_{ca}\Omega_{da}}{8\Delta_{cg}\Delta_{ag}\Delta_{dg}}\rho_{gg}\exp(i[[(k_1 - k_2 + k_3)z$$
$$- (\omega_1 - \omega_2 + \omega_3)t]), \tag{9}$$

where $\Delta_{ag} = \omega_{ag} - \omega_1 + \omega_2 - i\Gamma_{ag}$. The nonlinear DOVE polarization depends on the sum of the contributions from all the coherences:

$$P = NF[\mu_{eb}(\rho_{eb}^\alpha + \rho_{eb}^\beta) + \mu_{dg}\rho_{dg} + \text{c.c.}], \tag{10}$$

where N is the total concentration of molecules, F is the local field correction factor, and μ_{ij} is the transition dipole moment for the ρ_{ij} coherence.

Fig. 3 shows the simulated 2D spectra for the three individual pathways. The two spectra from the two DOVE-IR pathways are asymmetric on an ω_2 vs. ω_1 plot because they both contain a resonance from the ρ_{cb} coherence that depends on $\omega_1 - \omega_2$ but they differ because one has an additional resonance that depends on ω_1 while the other depends on ω_2. The DOVE-Raman pathway is also asymmetric because one resonance depends only on ω_1 and the other depends on $\omega_1 - \omega_2$. The DOVE-IR pathways can be isolated from each other by using short excitation pulses that are time ordered to pick the particular pathway.

If the excitation pulses overlap in time, there are interesting changes in line shape that result from interference between pathways. Our treatment mirrors that of Tokmakoff in describing stimulated vibrational echoes [46]. The relative contributions depend upon the dephasing rates of the coherences in each pathway. If the two DOVE-IR contributions are added, Eqs. (7) and (8) can be combined to give the expression:

$$\rho_{eb} = \frac{\Omega_{gc}\Omega_{ce}\Omega_{gb}}{8\Delta_{cg}\Delta_{bg}^*\Delta_{eb}}\left(1 + \frac{i(\Gamma_{cb} - \Gamma_{cg} - \Gamma_{bg})}{\Delta_{cb}}\right)\rho_{gg}$$
$$\times \exp(i[[(k_1 - k_2 + k_3)z - (\omega_1 - \omega_2 + \omega_3)t]). \tag{11}$$

(a) gg→cg→cb→db DOVE-IR
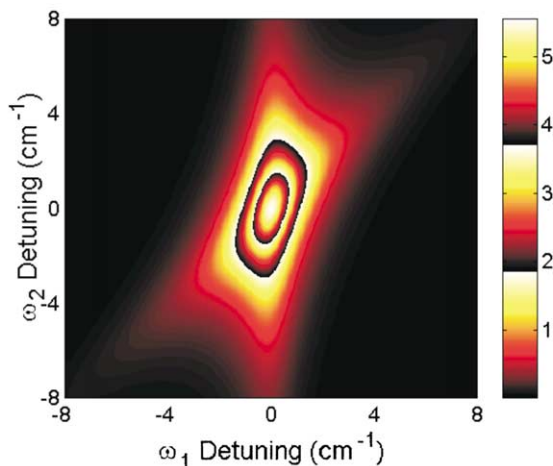
(b) gg→gb→cb→db DOVE-IR
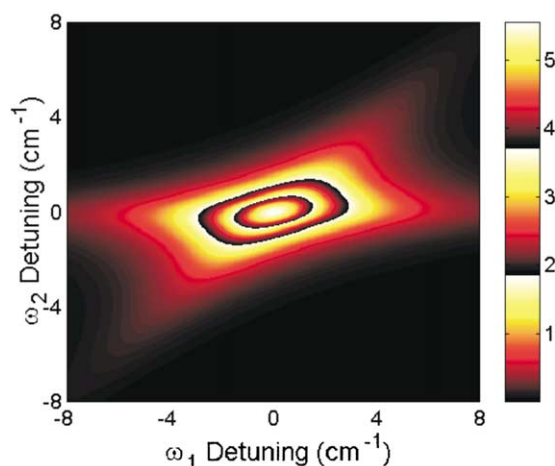
(c) gg→cg→ag→dg DOVE-Raman
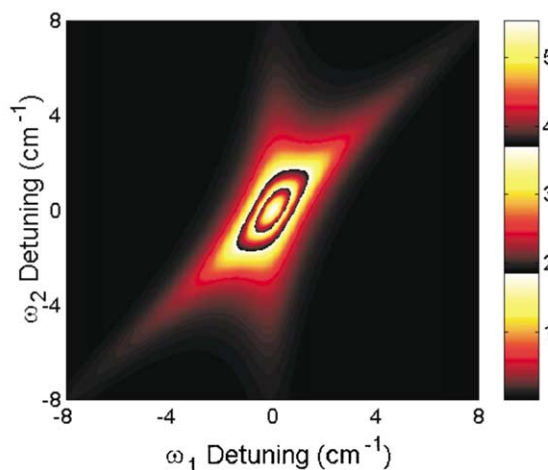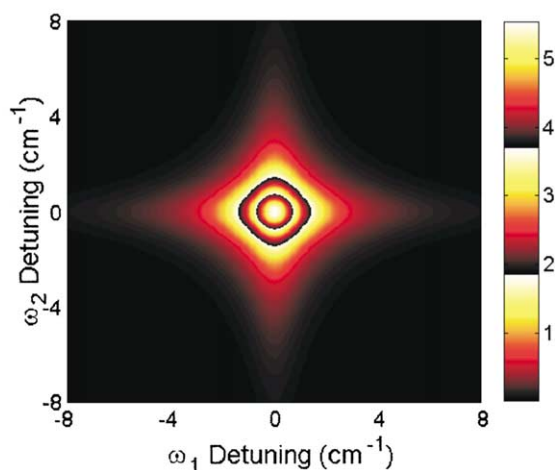

(d) Interference between (a) and (b)

Fig. 3. Characteristic 2D spectra for each major contributing pathways to the 2D DOVE signal. We assume $\Gamma_{cg} = \Gamma_{bg} = \Gamma_{ag} = \Gamma_{cb}/2 = 1$: (a) gg → cg → cb → eb DOVE-IR pathway, (b) gg → gb → cb → eb DOVE-IR pathway, (c) gg → cg → ag → dg DOVE-Raman pathway, (d) interference between pathways (a) and (b).

The second term is usually referred to as a dephasing induced resonance [47,48] and for vibrational spectroscopies, it should be very important. Its importance is determined by the dephasing rates of the states involved in the transitions. Fig. 3d shows the 2D Lorentzian that results when the second term goes to zero. For DOVE spectroscopies where the modes are coupled, the dephasing rates for the c → b, c → g, b → g, and a → g transitions are related and the second term may not go to zero.

For the DOVE experiment there are six nonlinear polarizations that are important and each has a characteristic frequency dependence. The third order frequency domain hyperpolarizability γ can be written as:

$$\gamma = \sum_{a,b,c\,=\,\text{all states}} \frac{A_{cg}^{(1)}}{\Delta_{cg}} + \frac{A_{bg}^{(2)}}{\Delta_{bg}^*} + \frac{A_{cg,bg}^{(3)}}{\Delta_{cg}\Delta_{bg}^*}$$

$$\times \left(1 + \frac{i\left(\Gamma_{cb} - \Gamma_{cg} - \Gamma_{bg}\right)}{\Delta_{cb}}\right) + \frac{A_{cg,ag}^{(4)}}{\Delta_{cg}\Delta_{ag}}$$

$$+ \frac{A_{ag}^{(5)}}{\Delta_{ag}} + A^{(6)}, \qquad (12)$$

where the first two terms describe SIVE processes caused by the IR absorption transitions at ω_1 or ω_2 [42], the third term describes the DOVE-IR-FWM process with two IR absorption transitions, the fourth term describes the DOVE-Raman-FWM process, the fifth term describes ordinary coherent Raman processes, and the last term describes nonresonant processes [10,11]. The numerators each contain four transition moments and electronic resonance factors that control the importance of each contribution.

2.2. Dephasing and mode coupling effects

The relationships between the dephasing rates of the states involved in the DOVE transitions require a consideration of the mode coupling effects. If there is no mode coupling, the vibrational transitions involve states where a vibrational quantum number change is $\Delta v = \pm 1$. However, double resonances require changes in the quantum numbers of two modes so the transition moments in the Rabi frequencies of Eqs. (9) and (11) must involve mode coupling if the processes are observable. The transitions therefore must involve at least one combination band in the IR or Raman transitions.

For DOVE-IR, the mode coupling can occur in the IR absorption transitions $g \rightarrow b$, $g \rightarrow c$, and/or the Raman transition $c \rightarrow b$ (see Fig. 2). For DOVE-Raman, the mode coupling can occur in the IR absorption transitions $g \rightarrow c$, the infrared emission $c \rightarrow a$, and/or the Raman transition $a \rightarrow g$. Transitions can be described by the notation $|v_1, v_2\rangle \rightarrow |v_1', v_2'\rangle$. Figs. 4 and 5 visualize examples of different combinations of transitions for DOVE-IR and DOVE-Raman, respectively (there are also a similar series of diagrams that are not shown where the definitions of v_1 and v_2 are in-

terchanged). The first three cases correspond to the different orderings of having one combination band transition and two fundamental transitions. The next four cases correspond to the different orderings of having two combination bands and one fundamental transition. The last case corre-
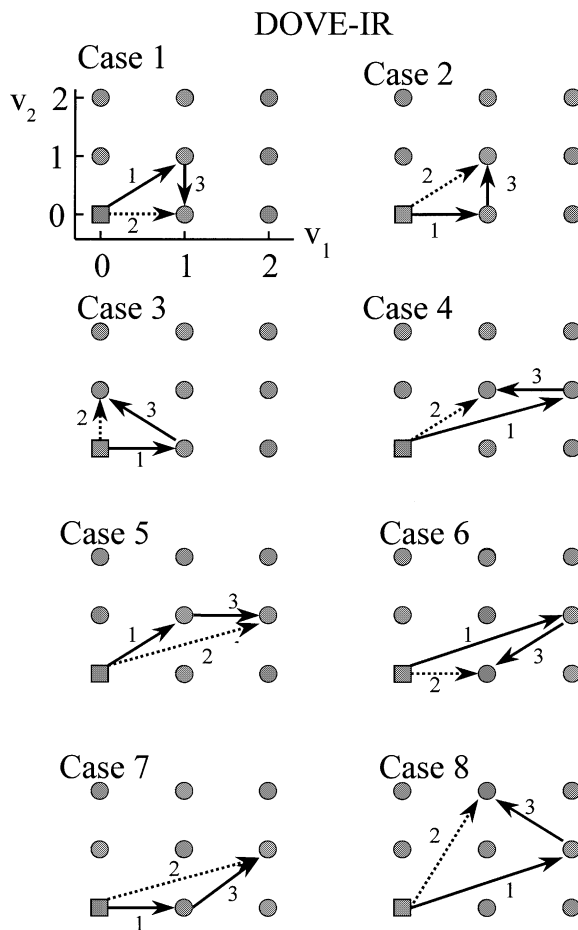

Fig. 4. The figure shows the changes in the vibrational quantum numbers in two modes (v_1 and v_2) for the two IR absorption transitions (labeled as 1 and 2) and the Raman transition (labeled as 3) that together make a DOVE-IR process. The top left indicates the vibrational states considered. Fundamental transitions are indicated by horizontal and vertical arrows with $\Delta v = \pm 1$. Combination bands are indicated by diagonal arrows. The eight cases show examples of possible transitions for three transitions involving one, two, or three combination bands. The solid and dotted arrows indicate ket- and bra-side transitions, respectively. A square indicates the initial state.
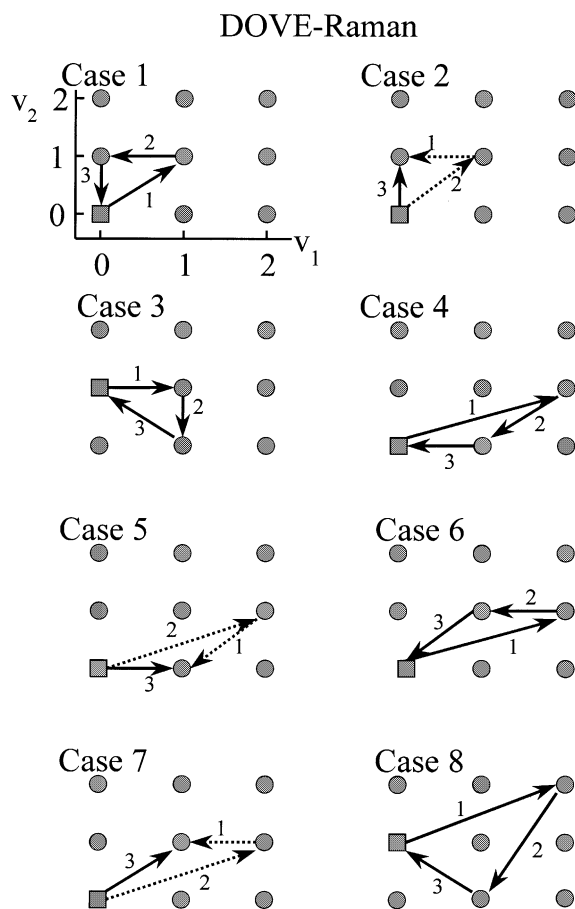
DOVE-Raman

Fig. 5. The figure shows the changes in the vibrational quantum numbers in two modes (v_1 and v_2) for the IR absorption and emission transitions (labeled as 1 and 2, respectively) and the Raman transition (labeled as 3) that together make a DOVE-Raman process. The top left indicates the vibrational states considered. Fundamental transitions are indicated by horizontal and vertical arrows with $\Delta v = \pm 1$. Combination bands are indicated by diagonal arrows. The eight cases show examples of possible transitions involving one, two, or three combination bands. The solid and dotted arrows indicate ket- and bra-side transitions, respectively. A square indicates the initial state. The cases are chosen to parallel similar transitions for DOVE-IR cases.

sponds to three combination band transitions. The Δv values chosen have been minimized for each example. The DOVE-Raman examples have been chosen to have similar transitions to the DOVE-IR examples. Solid and dotted arrows indicate ket- and bra-side transitions, respectively, and squares indicate the initially populated state. In our work,

the transitions in Figs. 4 and 5 are labeled 1 and 2 and correspond to the IR transitions initiated by laser frequencies ω_1 and ω_2, respectively, while transition 3 corresponds to the Raman transition involving frequencies 3 and 4 in Fig. 2. Overtone transitions can be included by straightforward extension.

As an example, consider case 1 for DOVE-IR (Fig. 4). The two IR transitions involve $|00\rangle \rightarrow |11\rangle$ for the combination band ($\Delta v_1 = 1$ and $\Delta v_2 = 1$) and $|00\rangle \rightarrow |10\rangle$ ($\Delta v_1 = 1$, $v_2 = 0$) for the fundamental, while the Raman transition (transition 3 in Fig. 4) involves $|11\rangle \rightarrow |10\rangle$ ($v_1 = 1$, $\Delta v_2 = -1$). The cross-peak occurs when $\omega_1 = \omega_{v1} + \omega_{v2} - \delta$ and $\omega_2 = \omega_{v1}$ where δ is the anharmonicity for the combination band (ω_{v1} and ω_{v2} indicate the energies for the two modes). For case 1 with DOVE-Raman (Fig. 5), the first two IR transitions involve $|00\rangle \rightarrow |11\rangle$ for the combination band ($\Delta v_1 = 1$ and $\Delta v_2 = 1$) and $|11\rangle \rightarrow |01\rangle$ ($\Delta v_1 = -1$, $v_2 = 1$) for the fundamental while the Raman transition involves $|01\rangle \rightarrow |00\rangle$ ($v_1 = 0$, $\Delta v_2 = -1$). Note that the transitions for the DOVE-Raman process are very similar to the DOVE-IR process. The only differences are the quantum number of the state that is not changing in the transitions and the sign of Δv. The cross-peak occurs when $\omega_1 = \omega_{v1} + \omega_{v2} - \delta$ and $\omega_1 - \omega_2 = \omega_{v2}$ or $\omega_2 = \omega_{v1} - \delta$. The cross-peaks for DOVE-IR and DOVE-Raman are off-set along the ω_2 axis by δ so they are usually close enough to interfere.

On the other hand, consider case 3 for DOVE-IR. The two IR transitions are both fundamentals involving $|00\rangle \rightarrow |10\rangle$ ($\Delta v_1 = 1$, $v_2 = 0$) and $|00\rangle \rightarrow |01\rangle$ ($v_1 = 0$, $\Delta v_2 = 1$) while the Raman transition involves $|10\rangle \rightarrow |01\rangle$ combination band transition ($\Delta v_1 = -1$ and $\Delta v_2 = 1$). The cross-peak occurs when ω_1 and ω_2 are resonant with ω_{v1} and ω_{v2}. For case 3 with DOVE-Raman, it is not possible to involve similar transitions from a populated ground state. Instead, one must start from an excited vibrational state (see Fig. 5, case 3). In this example, the two IR transitions involve the $|01\rangle \rightarrow |11\rangle$ fundamental absorption ($\Delta v_1 = 1$ while $v_2 = 1$), the $|11\rangle \rightarrow |10\rangle$ fundamental emission ($v_1 = 1$ and $\Delta v_2 = -1$) and the Raman transition $|10\rangle \rightarrow |01\rangle$ combination band ($\Delta v_1 = -1$

Table 1
Summary of the pure dephasing relationships in the limit of no correlation and complete correlation in the pure dephasing rates

	No correlation	Complete correlation
Γ_{ag}^*	$(A_a^2 + A_g^2)\Phi$	$(A_a - A_g)^2\Phi$
Γ_{cg}^*	$\Gamma_{ag}^* + \Gamma_{bg}^* + 2A_g^2\Phi$	$\Gamma_{ag}^* + \Gamma_{bg}^* + 2\sqrt{\Gamma_{ag}^*\Gamma_{bg}^*}$
Γ_{ba}^*	$\Gamma_{ag}^* + \Gamma_{bg}^* - 2A_g^2\Phi$	$\Gamma_{ag}^* + \Gamma_{bg}^* - 2\sqrt{\Gamma_{ag}^*\Gamma_{bg}^*}$
Γ_{cb}^*	Γ_{ag}^*	Γ_{ag}^*
$\Gamma_{ba}^* - \Gamma_{bg}^* - \Gamma_{ag}^*$	$-2A_g^2\Phi$	$-2\sqrt{\Gamma_{ag}^*\Gamma_{bg}^*}$
$\Gamma_{cb}^* - \Gamma_{bg}^* - \Gamma_{cg}^*$	$-2\Gamma_{bg}^* - 2A_g^2\Phi$	$-2\Gamma_{bg}^* - 2\sqrt{\Gamma_{ag}^*\Gamma_{bg}^*}$

State c is a combination band of states b and a.

while $v_2 = 1$). This process will be weak at room temperature and will not interfere. There are usually other DOVE-Raman processes that have initial ground state populations and involve other vibrational states but these are displaced in frequency from the DOVE-IR peak so they are not considered in this treatment.

For this paper, we are interested in case 1 where one of the IR absorption transitions of DOVE-IR is a combination band and the other transitions are fundamentals. For this case, the a and b states are different vibrational modes and state c is a combination band of states a and b. The pure dephasing rate for the i → j transition is

$$\Gamma_{ij}^* = \int_0^\infty d\tau\, [\Delta\omega_i(\tau) - \Delta\omega_j(\tau)][\Delta\omega_i(0) - \Delta\omega_j(0)],$$
(13)

where the $\Delta\omega_i(\tau)$ represent the instantaneous frequency fluctuations about the mean ω_i frequency. We define $\Delta\omega_i(t) = A_i\phi_i(t)$, where $\phi(t)$ is a stochastic function such that $\langle\phi_i(t)\phi_i(0)\rangle = 1$ when $t = 0$. With this definition, the pure dephasing rates for the important transitions are:

- $\Gamma_{ag}^* = A_a^2\Phi_{aa} + A_g^2\Phi_{gg} - A_aA_g(\Phi_{ag} + \Phi_{ga})$ for the fundamental g → a transition (a similar expression can be written for the fundamental g → b transition, Γ_{bg}^*),
- $\Gamma_{cg}^* = \Gamma_{ag}^* + \Gamma_{bg}^* + 2A_g^2\Phi_{gg} + A_aA_b(\Phi_{ab} + \Phi_{ba}) - A_aA_g(\Phi_{ag} + \Phi_{ga}) - A_bA_g(\Phi_{bg} + \Phi_{gb})$ for the g → c combination band,
- $\Gamma_{ba}^* = \Gamma_{ag}^* + \Gamma_{bg}^* + 2A_g^2\Phi_{gg} - A_aA_b(\Phi_{ab} + \Phi_{ba}) + A_aA_g(\Phi_{ag} + \Phi_{ga}) + A_bA_g(\Phi_{bg} + \Phi_{gb})$ for the ρ_{ba} coherence, and

- $\Gamma_{cb}^* = \Gamma_{ag}^*$ for the ρ_{cb} coherence.
  In each case, $\Phi_{ij} \equiv \int_0^\infty d\tau\langle\phi_i(\tau)\phi_j(0)\rangle$.

There are two limits for these expressions: (1) no correlations so $\Phi_{ij} = \Phi\delta_{i,j}$ and (2) complete correlation so $\Phi_{ij} = \Phi$ (a constant). Table 1 summarizes the pure dephasing rates for the different transitions, coherences, and the combinations of dephasing rates in these two limits. A discussion of the line shapes that result from different parameter choices is presented in the discussion of the experimental data.

3. Experimental

The sample for this experiment was a 100 μm thick (35:35:3 mol%) mixture of acetonitrile, deuteroacetonitrile, and deuterobenzene. It was contained within a rectangular capillary with 100 μm thick walls. The double resonance involved two IR regions – one near acetonitrile IR v_2 C≡N stretch fundamental at 2253 cm^{-1} and the other near the $v_2 + v_4$ combination band (C≡N and C–C stretch) at 3164 cm^{-1}. This level structure corresponds to the case 1 example in the theoretical section. The deuterobenzene also had a Raman transition for the ring breathing mode at $\omega_1 - \omega_2 = 944$ cm^{-1} in the same region of the scans.

The DOVE experiments were performed using an injection seeded Nd:YAG laser to excite two laser vision optical parametric oscillator/amplifier (OPO/OPA) systems based on KTP/KTA nonlinear crystals. The bandwidth of the IR output from the OPO/OPA's was determined by the phase matching and was typically ~2 cm^{-1}. The IR fre-

quencies, labeled ω_1 and ω_2, were controlled by a computer. The intensities of the ω_1 and ω_2 beams were measured during all scans and the signal intensity was corrected for any variations. The frequencies of the two OPO/OPA's were measured using a hollow cathode lamp and the optogalvanic effect.

problems is amplitude level interference between the nonresonant background of the sample and the windows of the sample cell. These have been described in more detail elsewhere [45]. Briefly, the electric field at ω_4 that results from a sample cell with an input and output window is

$$E^0 = \frac{2\pi i \omega_4 E_1^0 E_2^0 E_3^0 t_4^{wa} t_{123}^{aw}}{c} \left[\frac{\chi_s^{(3)} F_{4s} M_s t_4^{sw} t_{123}^{ws} l_s \exp\left(i\Delta k_w l_w - \Delta \alpha_w l_w\right)}{n_{4s}} \right.$$
$$\left. + \frac{\chi_w^{(3)} F_{4w} M_w l_w \left(t_{123}^{ws} t_{123}^{sw} \exp\left(i\Delta k_w l_w - \Delta \alpha_w l_w\right) \exp\left(i\Delta k_s l_s - \Delta \alpha_s l_s\right) + t_4^{ws} t_4^{sw}\right)}{n_{4w}} \right], \tag{14}$$

The two IR beams were focused into the sample along with the doubled 532 nm output (ω_3) of the Nd:YAG laser. The ω_1 and ω_3 beams were almost collinear and the ω_2 beam was directed at an 8° angle for optimum phase matching. The output beam at $\omega_4 = \omega_1 - \omega_2 + \omega_3$ was spatially isolated with an aperture and spectrally isolated with a holographic filter and a double monochromator. The monochromator was scanned in synchronization with the ω_1 frequency for different fixed settings of the ω_2 frequency. This scanning strategy was chosen to avoid the large changes in absorption and refractive index that would be associated with a scan of ω_2 in the region of the strong v_2 modes [41,45]. The strong v_2 absorptions still have an effect on the spectra when ω_1 is scanned, depending upon the choice of ω_2, but the effects are the same throughout each scan. The effect of the weaker absorption and refractive index changes for different ω_2 values was included in the modeling. The deuterobenzene CARS resonance at 944 cm^{-1} serves as a standard of constant $\chi^{(3)}$ that normalize the output intensity for each scan. Even though there are also absorption resonances in the region of $v_2 + v_4$, they are weak and do not cause large changes in absorption or refractive index.

Nonlinear spectroscopy is sufficiently complex that artifacts can be mistaken for multidimensional spectral features, so it is important to eliminate them before observations can be considered definitive. One of the more insidious

where $M_x = (\exp((i\Delta k_x - \Delta \alpha_x) l_x) - 1)/((i\Delta k_x - \Delta \alpha_x) l_x)$, $\Delta \alpha_x = \alpha_{1,x} + \alpha_{2,x} + \alpha_{3,x} - \alpha_{4,x}$, $\alpha_{i,x}$ and $n_{i,x}$ are the absorption coefficient and index of refraction at ω_i for either the air, windows, or sample (labeled a, w or s), l_x is the pathlength, $t_i^{xx'} = 2n_{i,x}/(n_{i,x} + n_{i,x'})$ and $t_{123}^{wa} = t_1^{wa} t_2^{wa} t_3^{wa}$. Normally, one expects the nonresonant $\chi^{(3)}$ to be real and enter as a constant background in spectral simulations. The window contribution can then be subtracted from the spectrum without any effect on the line shape. However, since it is not possible to phase match the windows and sample simultaneously, Δk will not be zero for the windows and the M factor will make the window contributions complex. Now the window contribution will be different from the sample nonresonant background and it will cause interferences that change the line shape. A simple subtraction of the nonresonant background is no longer sufficient. Fig. 6 shows example simulations of the effects. In Fig. 6a, the windows and sample were modeled to have only a constant and real nonresonant $\chi^{(3)}$ without any DOVE features but the acetonitrile absorption and refractive index changes were included for the sample and sample cell. In Fig. 6b, we have removed the window contribution. In each case, one has a spectrum that appears to be a 2D vibrational spectrum, but in actuality there are only one-dimensional (1D) absorption and refractive index effects. These types of artifacts were first observed by Ender et al. from FWM in rare earth doped crystals [49].
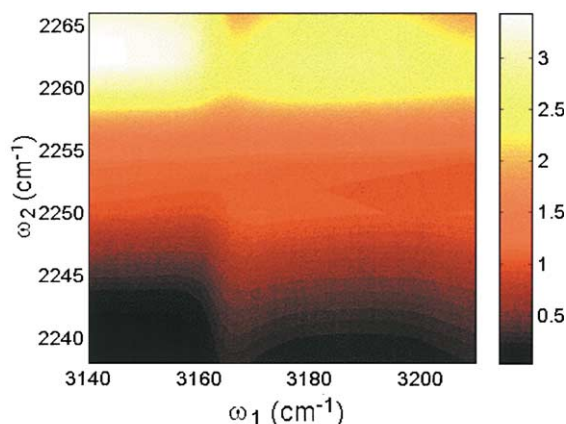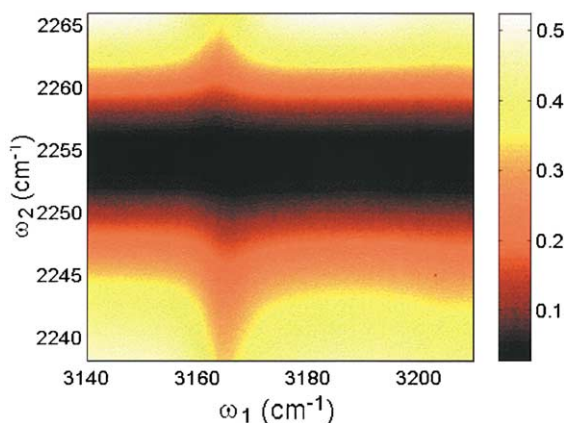
(a) Simulation of M_S and M_W effects

(b) Simulation of M_S without windows effects

Fig. 6. (a) Simulation of the nonresonant background in a 2D spectrum with corrections for the effects of absorption and refractive index dispersion through M_s and M_w. (b) Simulation of the nonresonant background in a 2D spectrum with corrections for the effects of absorption and refractive index dispersion through M_s but $M_w = 0$.

4. Results and discussion

Fig. 7 shows the absorption and Raman spectra of acetonitrile in the regions of interest for this work. One can see the strongest absorption line is the v_2 C≡N stretch and the strongest Raman feature is the v_4 C–C stretch mode. The symmetric and asymmetric v_1 and v_5 C–H stretch modes are also in the region of interest. In addition, the $v_3 + v_4$, $v_2 + v_4$, and $v_3 + 2v_4$ combination bands are important for this work.

Fig. 8 shows the 2D contour plot of the DOVE spectrum for scans of the ω_1 frequency and different choices of the ω_2 frequency. There are three color cycles to better show the baseline features as well as the peak shapes. The central peak is assigned to the DOVE IR process for ω_1 resonant with the $v_2 + v_4$ combination band at 3164 cm^{-1} and ω_2 resonant with the v_2 C≡N stretch mode at 2255 cm^{-1}. The tail on the lower part of the peak is assigned to the DOVE-Raman process for ω_1 resonant with the $v_2 + v_4$ combination band at 3164 cm^{-1} and $\omega_1 - \omega_2$ resonant with the v_4 C–C stretch mode at 917 cm^{-1}. The two features are offset by $\Delta\omega_2 = 6$ cm^{-1} because of the anharmonicity. The diagonal line on the right is assigned to the deuterobenzene resonance at $\omega_1 - \omega_2 = 944$ cm^{-1}.

When ω_2 is far from vibrational features, the spectrum is dominated by the diagonal acetonitrile v_4 Raman line at 917 cm^{-1} and deuterobenzene Raman line at 944 cm^{-1}. The relative intensities of these lines are independent of the ω_2 value as long as there are no vibrational resonances nearby. As one nears the v_2 mode, there is an enhancement in the v_4 mode from the DOVE-Raman and the new feature, the main DOVE-IR peak, appears and grows in intensity. There is a competition in this region between the enhancement in the FWM from the DOVE resonances and the attenuation of the excitation beams that limits the mixing pathlength and decreases the absolute signal. Absorption effects are controlled by the M factor in Eq. (14). The effects are minimized by choosing shorter sample pathlengths. Since the deuterobenzene Raman line is not affected by enhancements in this region, its nonlinearity remains constant and serves as an internal reference. In order to reduce the effects of drifts in signal intensity and to correct for the changes in absorption and refractive index at different ω_2 values, all the ω_1 scans were normalized relative to the deuterobenzene Raman line intensity.

It is interesting to compare the experimental line shape with that expected from the theoretical treatment. Fig. 9 shows the line shapes that result from changing the dephasing rates, Γ_{bg}, Γ_{cg}, and Γ_{cb}. The relative dephasing rates control the contributions from each coherent pathway in DOVE-
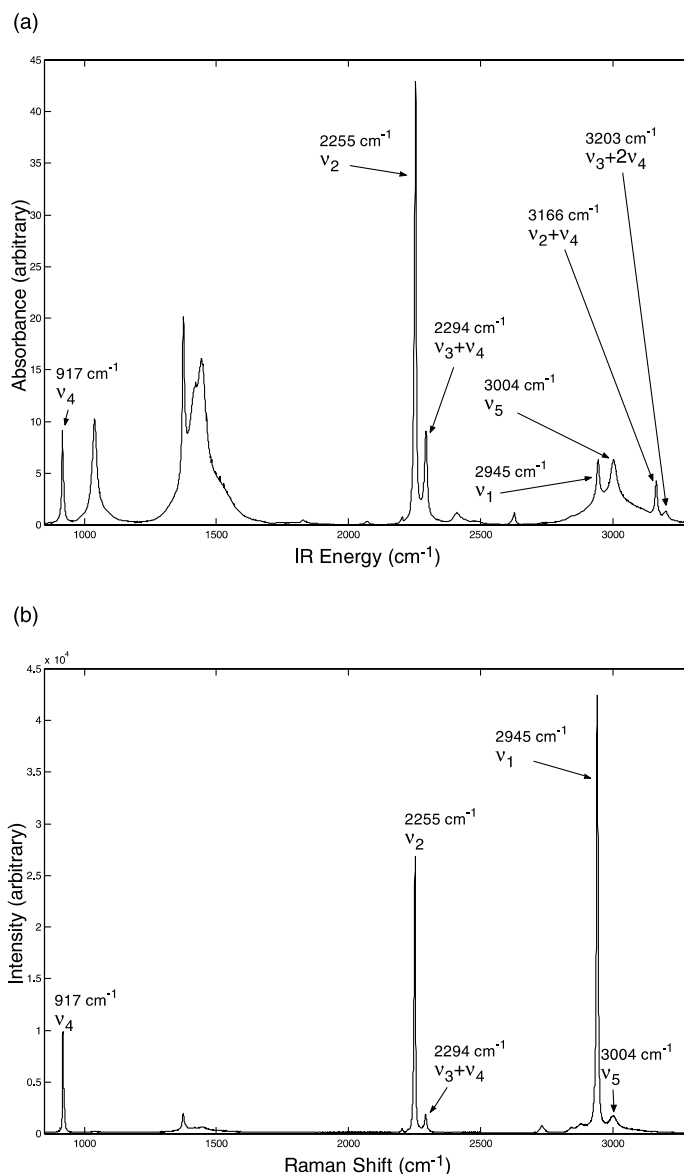
(a)

(b)

Fig. 7. 1D spectra of CH$_3$CN: (a) IR absorption and (b) Raman.

IR and therefore control the interferences that are responsible for the line shape. We have chosen parameter values that are appropriate for the acetonitrile, deuteroacetonitrile, and deuterobenzene sample discussed in the experimental section. In particular, we have chosen values for the DOVE-IR and DOVE-Raman magnitudes ($A^{(3)}$ and $A^{(4)}$ in Eq. (12), respectively) and the Γ_{bg} and Γ_{cg} dephasing rates that provide the best match with experiment [10,11]. The Γ_{cb} is not directly measured and must be inferred from the data. We have included the absorption and refractive index dispersion that control phase matching. We have also assumed that the dephasing rates are dominated by the pure dephasing contribution since the lifetime contribution is appreciably smaller [50,51].
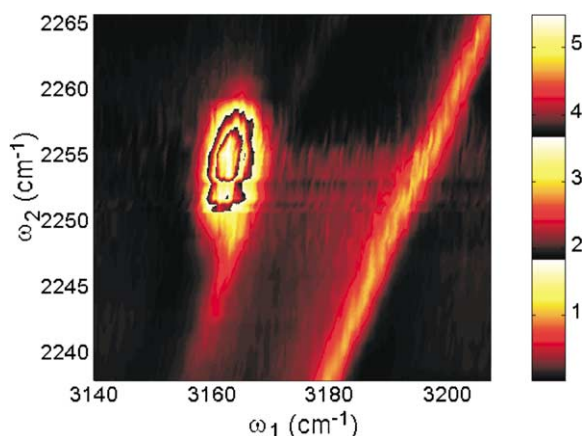
Fig. 8. Experimental 2D DOVE spectrum of a CH_3CN, CD_3CN, C_6D_6 sample in the vicinity of the main peak. There is a three-cycle color bar to allow simultaneous viewing of intense and weak features.

It is instructive to simulate the 2D spectrum expected in the limit where $\Gamma_{cb}^* - \Gamma_{bg}^* - \Gamma_{cg}^* - \Gamma_{gg} = \Gamma_{cb} - \Gamma_{bg} - \Gamma_{cg} = 0$ so, given our experimental values for Γ_{bg} and Γ_{cg}, Γ_{cb} is 5.2 cm^{-1} (see Table 2). The no pure dephasing limit is an example of such a condition [47,48]. The resulting 2D spectrum is shown in Fig. 9a. The line shape of the DOVE-IR feature would be the diamond-shaped Lorentzian that is usually associated with 2D vibrational spectroscopies [52–55], but the DOVE-Raman feature overlaps the lower right portion of the peak so it becomes distorted.

Table 1 shows a more realistic expectation for the Γ_{cb}^* dephasing rate is given by Γ_{ag}^*. For this case where the ρ_{cb} coherence involves the $v_2 + v_4$ combination band and the v_2 C≡N stretch, Γ_{cb} should be the dephasing rate of the v_4 C–C stretch mode, $\Gamma_{ag} = 2.5$ cm^{-1}, instead of that expected in the limit where Γ_{cb} is 5.2 cm^{-1}. Using this value for Γ_{cb} gives the simulation shown in Fig. 9b. The shape is much closer to the observed shape but it has more diagonal character than the experimental result.

There is another problem with the values required to approximate the experimental line shape. The magnitude of the DOVE-Raman contribution ($A^{(4)}$ in Table 2) that is required from fitting the data is 4× smaller than the DOVE-IR contribution ($A^{(3)}$ in Table 2). However, our preceding discussion of case 1 indicates that since the DOVE-

Raman and DOVE-IR transitions are so similar, one would expect their intensities to be roughly equal. Fig. 9c simulates the line shapes for the case where the DOVE-Raman and DOVE-IR are equal. The DOVE-Raman process appears as a diagonal peak on the DOVE-IR peak. It is offset from the DOVE-IR peak because of the anharmonicity. Note that it is more dominate in the Fig. 9c simulation than Fig. 9b and it is clearly too large to agree with the observed line shape.

The line shapes can also be distorted by the absorption and refractive index effects. In order to show the magnitude of these contributions, Fig. 9 shows a simulation of the 2D DOVE spectra of the CH_3CN, CD_3CN, C_6D_6 sample with (Fig. 9b) and without (Fig. 9d) the absorption and refractive index effects of the windows and sample included explicitly. Although they make an important contribution, they do not improve the agreement with the experimental line shapes.

The 2D vibrational spectrum only shows DOVE peaks that have appreciable mode coupling. For example, previous work observed two other DOVE-IR peaks, one when ω_1 was resonant with the $v_2 + v_4$ combination band and ω_2 was resonant with the $v_3 + v_4$ mode (v_3 involves the acetonitrile C–H bond) and the other when ω_1 was resonant with the $v_3 + 2v_4$ combination band and ω_2 was resonant with the $v_3 + v_4$ mode. In both cases, the double resonances involve IR combination bands that are strong because of mode coupling, either between v_2 and v_4 or v_3 and v_4. For the DOVE-IR v_2 and $v_2 + v_4$ double resonance, the combination band involves the $|00\rangle \rightarrow |11\rangle$ IR absorption transition ($|v_2v_4\rangle$). This is an example of a case 1 double resonance. For the DOVE-IR $v_3 + v_4$ and $v_3 + 2v_4$ double resonance, the combination bands include the $|00\rangle \rightarrow |11\rangle$ and the $|00\rangle \rightarrow |12\rangle$ IR absorption transitions (where $|ij\rangle$ indicates $|v_3v_4\rangle$). This is an example of a case 4 double resonance, except that v_1 and v_2 are interchanged. In both cases, the coupled modes involve adjacent bonds (C≡N and C–C stretch or C–C stretch and C–H bond) so one might expect that mechanical anharmonicities might be important. The other transitions required in the DOVE processes for these two double resonances all involve single vibrational quantum number changes.
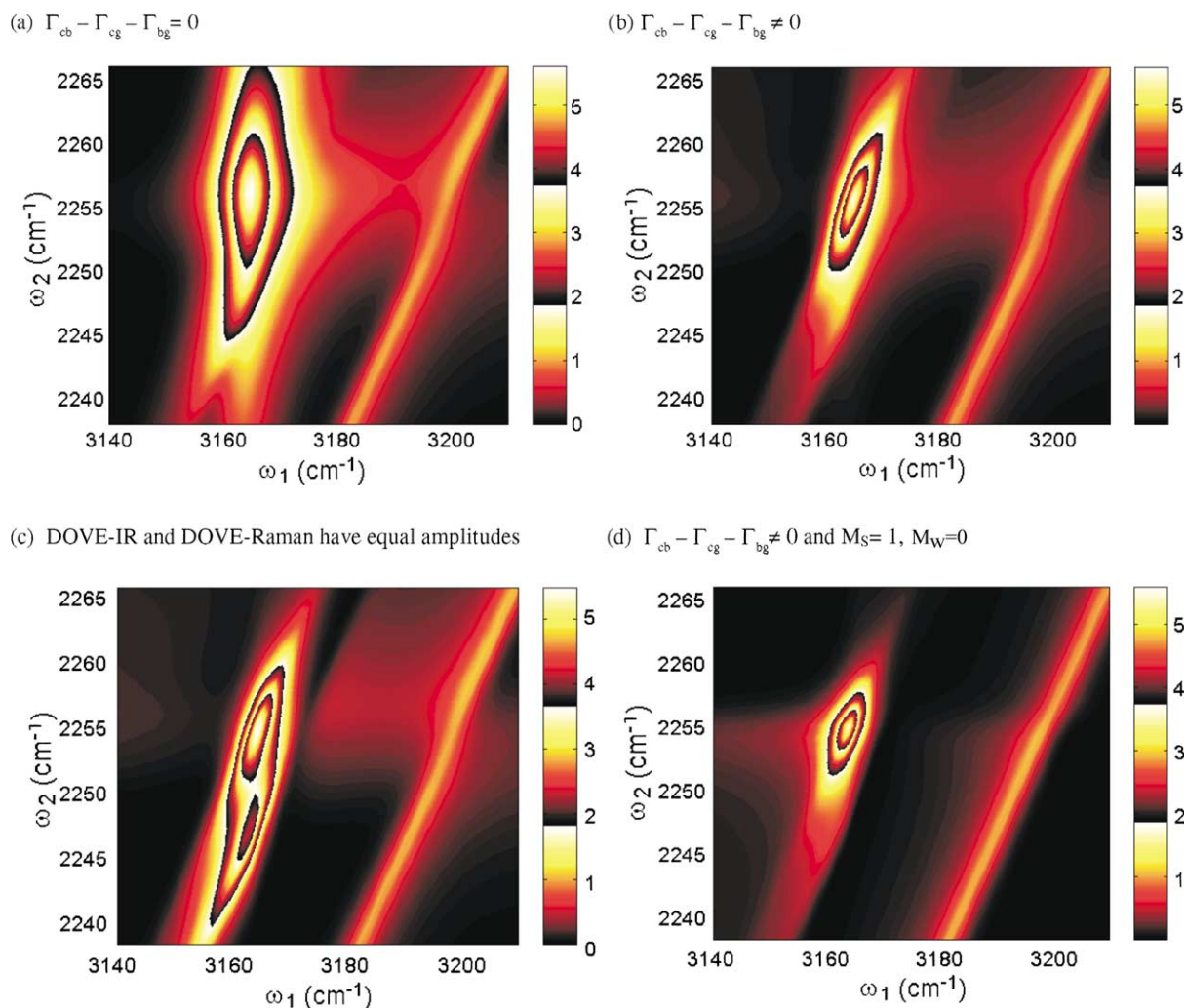
Fig. 9. Simulations of the main peak in 2D DOVE spectra for a CH_3CN, CD_3CN, C_6D_6 sample. The diagonal feature on the right is the 944 cm^{-1} C_6D_6 Raman resonance that is used as an internal intensity standard against which the other features are normalized. The simulation parameters are summarized in Table 2. (a) The Γ_{cb} parameter was chosen so $\Gamma_{cb} - \Gamma_{cg} - \Gamma_{bg} = 0$. (b) The Γ_{cb} parameter was chosen so $\Gamma_{cb} = \Gamma_{ag}$. (c) The same parameters were chosen as (b) but the DOVE-Raman and DOVE-IR amplitudes are equal. (d) The same parameters were chosen as (b) but $M_w = 0$ and $M_s = 1$.

Similar considerations hold for the DOVE-Raman processes. Table 3 summarizes the transitions that are important for DOVE-IR and DOVE-Raman processes for the two double resonance examples. Note that the DOVE-IR and DOVE-Raman transitions are very similar to each other and differ only in the quantum number of the mode that remains unchanged in the transition.

One should compare these processes with DOVE experiments on modes that are not cou-

pled. For example, the same spectral region has the possibility for achieving a double resonance involving the v_2 mode C≡N stretch mode and either the v_1 or v_5 C–H stretch modes. The DOVE-IR resonances would be a case 2 process (see Fig. 4). It would have two strong IR absorption transitions involving single vibrational quantum changes in the fundamentals, but it would also require a Raman combination band, where a C–H mode excitation was destroyed and a C≡N mode

Table 2
Summary of values used in simulations for Fig. 9

Common values for Fig. 9a–d			
Γ_{cg}	4.4 cm^{-1}	ω_{cg}	3164 cm^{-1}
Γ_{bg}	2.8 cm^{-1}	ω_{bg}	2255 cm^{-1}
Γ_{ag}	2.5 cm^{-1}	ω_{ag}	917 cm^{-1}
l_w	0.01 cm	$A_w^{(6)a}$	0.02
l_s	0.01 cm		
F	1.26		

CH$_3$CN		C$_6$D$_6$	
$A^{(1)a}$	0	$A^{(1)a}$	0
$A^{(2)a}$	0.02	$A^{(2)a}$	0
$A^{(5)a}$	0.02	$A^{(5)a}$	1
$A^{(6)a}$	0.013	$A^{(6)a}$	0.04

Values for specific parts of figure

Figure	Γ_{cb} (cm^{-1})	$A^{(3)a}$	$A^{(4)a}$
9a	5.2	0.19	0.045
9b	2.5	0.19	0.045
9c	2.5	0.19	0.19
9d	2.5	0.074[b]	0.045

[a] Value of A (see Eq. (12)) is normalized relative to the deuterobenzene 944 cm^{-1} line.
[b] Value required to make the main DOVE-IR feature equivalent to intensity in Fig. 9b.

excitation was created. Such a band is weak because the mode coupling is small. The C–H bond is separated from the C≡N bond by an intervening C–C bond so the anharmonicity is not as strong and combination bands are weak. Experimentally, we do not see any evidence for a DOVE feature at the appropriate frequencies.

The DOVE $\chi^{(3)}$ values can be determined by detailed fitting of the spectral line shapes in the 2D spectra using the known $\chi^{(3)}$ for the deuterobenzene Raman line at 944 cm^{-1} (we assume that deuterobenzene and benzene have the same values of $\chi^{(3)}$). The experimental procedure has been de-

scribed elsewhere [10,56,57]. The deuterobenzene Raman $\chi^{(3)}$ value must be corrected from the value measured by Levenson and Bloembergen [56,57] because of differences in the experiments. Levenson and Bloembergen used two lasers to generate an output at 525 nm for the CARS and measured a value of $\chi^{(3)} = 1.6 \times 10^{-13}$ cm^3 erg^{-1}. Our experiments use three lasers with very different frequencies so the $\chi^{(3)}$ is expected to change. The $\chi^{(3)}$ for a three-laser experiment is a factor of two different from a two-laser experiment in the Maker–Terhune convention for $\chi^{(3)}$. In addition, we calculated the expected change in $\chi^{(3)}$ from the frequencies used by Levenson and Bloembergen to the frequencies used in the DOVE experiments using the procedure described elsewhere [58]. The result is that the deuterobenzene $\chi^{(3)}$ used as a standard at the DOVE frequencies should be 11% smaller than the Levenson and Bloembergen value [10]. Using this value of 7.1×10^{-14} cm^3 erg^{-1} for the deuterobenzene Raman $\chi^{(3)}$, we obtain a value of 3.1×10^{-14} cm^3 erg^{-1} for the acetonitrile DOVE-IR resonance at $\omega_1 = 3164$ and $\omega_2 = 2253$ cm^{-1}, and 5.7×10^{-15} cm^3 erg^{-1} for the Raman resonance of acetonitrile at $\omega_1 - \omega_2 = 917$ cm^{-1}.

Our interpretation of the DOVE-IR resonance can be reinforced by calculating the value of the DOVE-IR $\chi^{(3)}$ from the absorption coefficients of the two IR absorption transitions and the $\chi^{(3)}$ of the final Raman transition. The IR absorption coefficient, Raman $\chi^{(3)}$, and DOVE $\chi^{(3)}$ are

$$\alpha_{bg} = \frac{4\pi\omega_{bg}NF_{bg}\mu_{bg}^2\rho_{gg}}{\hbar c \Gamma_{bg}}, \qquad (15)$$

$$\chi^{(3)}_{ag,\ Raman} = \frac{-iNF_{dg}^2F_{da}\mu_{dg}^2\mu_{da}^2\rho_{gg}}{4D_{Raman}h^3|\Delta_{dg}|^2\Gamma_{ag}}, \qquad (16)$$

Table 3
Changes in quantum numbers for different DOVE processes

	Transitions in $|v_2v_4\rangle$				Transitions in $|v_3v_4\rangle$			
	DOVE-IR	DOVE-Raman	Δv_2	Δv_4	DOVE-IR	DOVE-Raman	Δv_3	Δv_4
IR-absorption	$|00\rangle \to |11\rangle$	$|00\rangle \to |11\rangle$	+1	+1	$|00\rangle \to |12\rangle$	$|00\rangle \to |12\rangle$	+1	+2
IR-absorption/ stimulated emission	$|00\rangle \to |10\rangle$	$|11\rangle \to |01\rangle$	±1	0	$|00\rangle \to |11\rangle$	$|12\rangle \to |01\rangle$	±1	±1
Raman	$|11\rangle \to |10\rangle$	$|01\rangle \to |00\rangle$	0	−1	$|12\rangle \to |11\rangle$	$|01\rangle \to |00\rangle$	0	−z1

$$\chi_{\mathrm{DOVE}}^{(3)} = \frac{NF_{\mathrm{bg}}F_{\mathrm{cg}}F_{\mathrm{ce}}\mu_{\mathrm{cg}}\mu_{\mathrm{bg}}\mu_{\mathrm{ce}}\mu_{\mathrm{eb}}\rho_{\mathrm{gg}}}{4D_{\mathrm{DOVE}}h^3\Gamma_{\mathrm{bg}}\Gamma_{\mathrm{cg}}\Delta_{\mathrm{eb}}}\left(1 + \frac{\Gamma_{\mathrm{cb}}^{\mathrm{g}}}{\Gamma_{\mathrm{cb}}}\right). \tag{17}$$

Combining these expressions and a similar one for α_{cg}, we find

$$\chi_{\mathrm{DOVE}}^{3} = \frac{c\left(1 + \frac{\Gamma_{\mathrm{cb}}^{\mathrm{g}}}{\Gamma_{\mathrm{cb}}}\right)}{8\pi D_{\mathrm{DOVE}}}\sqrt{\frac{iF_{\mathrm{bg}}F_{\mathrm{cg}}D_{\mathrm{Raman}}\alpha_{\mathrm{bg}}\alpha_{\mathrm{cg}}\chi_{\mathrm{Raman}}^{(3)}\Gamma_{\mathrm{ag}}}{F_{\mathrm{eb}}\omega_{\mathrm{bg}}\omega_{\mathrm{cg}}\Gamma_{\mathrm{bg}}\Gamma_{\mathrm{cg}}\rho_{\mathrm{gg}}}}, \tag{18}$$

where $\Gamma_{\mathrm{cb}}^{\mathrm{g}} = \Gamma_{\mathrm{cb}} - \Gamma_{\mathrm{bg}} - \Gamma_{\mathrm{cg}}$, c is the speed of light, F is the local field factor, N is the number density, and D is a degeneracy factor. We used previously measured values of the absorption coefficient, α, for the $v_2 + v_4$ combination band and the v_2 fundamental band and the value reported above for $\chi_{\mathrm{Raman}}^{(3)}$ of acetonitrile. The $\chi_{\mathrm{Raman}}^{(3)}$ value was obtained at different frequencies than those used in this experiment, so again a correction must be made for the frequency dependence of $\chi_{\mathrm{Raman}}^{(3)}$. Since the correction is small, we use the same correction factor as benzene. These values are summarized elsewhere [10,11]. The calculations show that the predicted value for $\chi_{\mathrm{DOVE}}^{(3)}$ is 2.7×10^{-14} cm^3 erg^{-1}, in agreement with the measured value.

5. Conclusions

The frequency domain DOVE experiments provide experimental models for modeling the line shapes expected for multi-dimensional vibrational spectroscopy. They are closely related to other 2D vibrational methods and the insights that are obtained in understanding the DOVE spectra are likely to be useful for understanding other experiments as well. In addition, they can help to provide the fundamental foundations for developing this new field. We have shown in this paper that the dephasing effects have important effects on the line shape of a DOVE resonance. In particular, they change the characteristic diamond shape that is often predicted for 2D vibrational features [52–55], making it more elliptical and narrower. These changes are seen in the experimental spectra as well. However, the dispersion in the line shapes and the shapes of the features themselves still do not match those expected from these simple simulations. The simulations in this paper have not considered inhomogeneous broadening effects or the effect of the finite line widths of the excitation sources. These will be treated in a later publication.

2D coherent vibrational spectroscopy offers a new ability to probe the intramolecular and intermolecular interactions that control the behavior of any system. The DOVE experiments described in this paper were performed in the frequency domain, but it is clear that practical applications of DOVE methodologies in analytical measurements will require time domain femtosecond methods. The frequency domain experiments are limited by the nonresonant electronic background, which obscure the DOVE signals at low sample concentrations. Since the nonresonant background disappears on the time scale of the excitation lasers, the delay times that are possible with femtosecond time domain methods can remove the nonresonant background by including time delays that are long enough to remove the nonresonant background but shorter than the vibrational dephasing times so the signal intensity has not yet decayed [59]. The femtosecond pulses also allow higher instantaneous intensities that increase the nonlinear signals without inducing sample damage. In addition, the relative magnitudes of higher and lower order nonlinearities scales as Ω/Δ for each order of nonlinearity where Ω is the Rabi frequency and Δ is the resonance detuning factor. Thus, higher intensities produce higher Rabi frequencies that make the higher order nonlinearities more important. The multiple pulse experiments that are common in NMR might then become feasible if the effects of cascaded processes can be handled effectively.

References

[1] M.S. Sorem, A.L. Schawlow, Opt. Commun. 5 (1972) 148–152.

[2] M.D. Levenson, A.L. Schawlow, Phys. Rev. A A6 (1972) 10.

[3] T.W. Hansch, M.J. Nayfeh, S.A. Lee, S.M. Curry, I.S. Shahin, Phys. Rev. Lett. 32 (1974) 1336–1339.

[4] J.C. Wright, Applications of lasers in analytical chemistry, in: T.R. Evans (Ed.), Applications of Lasers to Chemical Problems, first ed., Wiley, New York, 1982, p. 35.

[5] L.A. Peteanu, R.W. Schoenlein, Q. Wang, R.A. Mathies, C.V. Shank, Proc. Natl. Acad. Sci. 90 (1993) 11762–11766.

[6] P. Hamm, M. Lim, R.M. Hochstrasser, J. Phys. Chem. B 102 (1998) 6123–6138.

[7] P. Hamm, M. Lim, W.F. DeGrado, R.M. Hochstrasser, Proc. Natl. Acad. Sci. 96 (1999) 2036–2041.

[8] J.C. Wright, R.J. Carlson, G.B. Hurst, J.K. Steehler, M.T. Riebe, B.B. Price, D.C. Nguyen, S.H. Lee, Int. Rev. Phys. Chem. 10 (1991) 349–390.

[9] J.C. Wright, P.C. Chen, J.P. Hamilton, A. Zilian, M.J. LaBuda, Appl. Spectrosc. 51 (1997) 949–958.

[10] W. Zhao, J.C. Wright, Phys. Rev. Lett. 83 (1999) 1950–1953.

[11] W. Zhao, J.C. Wright, Phys. Rev. 84 (2000) 1411–1414.

[12] P.L. DeCola, J.R. Andrews, R.M. Hochstrasser, H.P. Trommsdorff, J. Chem. Phys. 73 (1980) 4695–4696.

[13] S.H. Lee, J.K. Steehler, D.C. Nguyen, J.C. Wright, Appl. Spectrosc. 39 (1985) 243–253.

[14] J.K. Steehler, J.C. Wright, J. Chem. Phys. 83 (1985) 3188–3199.

[15] M.T. Riebe, J.C. Wright, Chem. Phys. Lett. 138 (1987) 565–570.

[16] M.T. Riebe, J.C. Wright, J. Chem. Phys. 88 (1988) 2981–2994.

[17] G.B. Hurst, J.C. Wright, J. Chem. Phys. 95 (1991) 1479–1486.

[18] G.B. Hurst, J.C. Wright, J. Chem. Phys. 97 (1992) 3940–3949.

[19] R.J. Carlson, D.C. Nguyen, J.C. Wright, J. Chem. Phys. 92 (1990) 1538–1546.

[20] R.J. Carlson, J.C. Wright, J. Chem. Phys. 92 (1990) 5186–5195.

[21] R.J. Carlson, J.C. Wright, J. Chem. Phys. 93 (1990) 2205–2216.

[22] R.J. Carlson, J.C. Wright, Anal. Chem. 63 (1991) 1449–1451.

[23] D.M. Bishop, E.K. Dalskov, J. Chem. Phys. 104 (1996) 1004–1011.

[24] C.W. Rella, A. Kwok, K. Rector, J.R. Hill, H.A. Schwettman, D.D. Dlott, M.D. Fayer, Phys. Rev. Lett. 77 (1996) 1648–1652.

[25] D. Zimdars, A. Tokmakoff, S. Chen, S.R. Greenfield, M.D. Fayer, T.I. Smith, H.A. Schwettman, Phys. Rev. 70 (1993) 2718–2722.

[26] P. Hamm, M. Lim, W.F. DeGrado, R.M. Hochstrasser, J. Phys. Chem. A 103 (1999) 10049–10053.

[27] W. Zhao, J.C. Wright, J. Am. Chem. Soc. 121 (1999) 10994–10998.

[28] G.M. Clore, A.M. Gronenborn, Science 252 (1991) 1390–1399.

[29] K. Wuthrich, Science 243 (1989) 45–50.

[30] C.K.N. Patel, R.E. Slusher, Phys. Rev. 29 (1968) 1087–1090.

[31] S. Mukamel, Principles of Nonlinear Optical Spectroscopy, first ed., Oxford University Press, New York, 1995, p. 543.

[32] J.E. Ivanecky, J.C. Wright, Chem. Phys. Lett. 206 (1993) 437–444.

[33] Y. Tanimura, S. Mukamel, J. Chem. Phys. 99 (1993) 9496–9511.

[34] K. Tominaga, K. Yoshihara, Phys. Rev. Lett. 74 (1995) 3061–3064.

[35] T. Steffen, K. Duppen, Phys. Rev. Lett. 76 (1996) 1224–1227.

[36] A. Tokmakoff, M.J. Lang, D.S. Larsen, G.R. Fleming, V. Chernyak, S. Mukamel, Phys. Rev. 79 (1997) 2702–2705.

[37] D.A. Blank, L.J. Kaufman, G.R. Fleming, J. Chem. Phys. 111 (1999) 3105–3114.

[38] D.A. Blank, L.J. Kaufman, G.R. Fleming, J. Chem. Phys. 113 (2000) 771–778.

[39] A. Zilian, M.J. LaBuda, J.P. Hamilton, J.C. Wright, J. Lumin. 60/61 (1994) 655–657.

[40] A. Zilian, M.J. LaBuda, J.P. Hamilton, J.C. Wright, J. Lumin. 60/61 (1994) 410–412.

[41] P.C. Chen, J.P. Hamilton, A. Zilian, M.J. Labuda, J.C. Wright, Appl. Spectrosc. 52 (1998) 380–392.

[42] M.J. Labuda, J.C. Wright, Phys. Rev. Lett. 79 (1997) 2446–2450.

[43] W. Zhao, K.M. Murdoch, D.M. Besemann, N.J. Condon, K.A. Meyer, J.C. Wright, Appl. Spectrosc. 54 (2000) 1000–1004.

[44] K.M. Murdoch, N.J. Condon, W. Zhao, D.M. Besemann, K.A. Meyer, J.C. Wright, Chem. Phys. (2000) submitted for publication.

[45] D.E. Thompson, J.C. Wright, J. Phys. Chem., accepted for publication.

[46] A. Tokmakoff, J. Phys. Chem. A 104 (2000) 4247–4255.

[47] Y. Prior, A.R. Bogdan, M. Dagenais, N. Bloembergen, Phys. Rev. 46 (1981) 111–114.

[48] J.R. Andrews, R.M. Hochstrasser, Chem. Phys. Lett. 83 (1981) 427–431.

[49] D.A. Ender, M.S. Otteson, R.L. Cone, M.B. Ritter, H.J. Guggenheim, Opt. Lett. 7 (1982) 611–616.

[50] J.C. Deak, L.K. Iwaki, D.D. Dlott, Chem. Phys. Lett. 293 (1998) 405–411.

[51] J.C. Deak, L.K. Iwaki, D.D. Dlott, J. Phys. Chem. A 102 (1998) 8193–8201.

[52] M. Cho, Two dimensional vibrational spectroscopy, in: S.H. Lin, A.A. Villaeys, Y. Fujimura (Eds.), Advances in Multi-Photon Processes and Spectroscopy, first ed., vol. 12, World Scientific, Singapore, 1999, pp. 1–72.

[53] M. Cho, J. Chem. Phys. 111 (1999) 4140–4147.

[54] K. Park, M. Cho, J. Chem. Phys. 109 (1998) 10559–10569.

[55] K. Park, M. Cho, J. Chem. Phys. 112 (2000) 5021–5036.

[56] M.D. Levenson, N. Bloembergen, J. Chem. Phys. 60 (1974) 1323–1327.

[57] M.D. Levenson, N. Bloembergen, Phys. Rev. B 10 (1974) 4447–4463.

[58] M.J. LaBuda, J.C. Wright, J. Chem. Phys. 108 (1998) 4112–4122.

[59] K.D. Rector, D. Zimdars, M.D. Fayer, J. Chem. Phys. 109 (1998) 5455–5465.